Observation of the fastest chemical processes in the radiolysis of water

Z.-H. Loh,[1*] G. Doumy,[2] C. Arnold,[3,4,5] L. Kjellsson,[6,7] S.H. Southworth,[2]
A. Al Haddad,[2] Y. Kumagai,[2] M.-F. Tu,[2] P.J. Ho,[2], A.M. March,[2]
R.D. Schaller,[8,9] M.S. Bin Mohd Yusof,[1] T. Debnath,[1] M. Simon,[10]
R. Welsch,[3,5] L. Inhester,[3] K. Khalili,[11] K. Nanda,[12] A.I. Krylov,[12]
S. Moeller,[13] G. Coslovich,[13] J. Koralek,[13] M.P. Minitti,[13] W.F. Schlotter,[13]
J.-E. Rubensson,[6], R. Santra,[3,4,5*] L. Young[2,14*]

[1]Division of Chemistry and Biological Chemistry, School of Physical and Mathematical Sciences,
Nanyang Technological University, Singapore
[2]Chemical Sciences and Engineering Division, Argonne National Laboratory, Lemont, IL USA
[3]Center for Free-Electron Laser Science, DESY, Hamburg, Germany
[4]Department of Physics, Universität Hamburg, Hamburg, Germany
[5]The Hamburg Centre for Ultrafast Imaging, Hamburg, Germany
[6]Department of Physics and Astronomy, Uppsala University, Uppsala, Sweden
[7]European XFEL GmbH, Schenefeld, Germany
[8]Center for Nanoscale Materials, Argonne National Laboratory, Lemont, IL, USA
[9]Department of Chemistry, Northwestern University, Evanston, IL, USA
[10]Sorbonne Université and CNRS, Laboratoire de
Chemie Physique-Matière et Rayonnement, LCPMR, F-750005, Paris, France
[11]Department of Energy Conversion and Storage,
Technical University of Denmark, Roskilde, Denmark
[12]Department of Chemistry, University of Southern California, Los Angeles, CA, USA
[13]LCLS, SLAC National Accelerator Laboratory, Menlo Park, CA, USA
[14]Department of Physics and James Franck Institute, The University of Chicago, Chicago, IL, USA

[*]To whom correspondence should be addressed;
E-mail: zhiheng@ntu.edu.sg, robin.santra@cfel.de, young@anl.gov

One sentence summary: Ultrafast x-rays capture the elementary steps of proton transfer and hydroxyl radical solvation in ionized liquid water.

Elementary processes associated with ionization of liquid water provide a framework for understanding radiation-matter interactions in chemistry and biology. While numerous studies have been conducted on the dynamics of the hydrated electron, its partner arising from ionization of liquid water, H_2O^+, remains elusive. We use tunable femtosecond soft x-ray pulses from an x-ray free electron laser to reveal the dynamics of the valence hole created by strong-field ionization and to track the primary proton transfer reaction giving rise to the formation of OH. The isolated resonance associated with the valence hole (H_2O^+/OH) enables straightforward detection. QM/MM calculations reveal that the x-ray spectra are sensitive to structural dynamics at the ionization site. We find signatures of hydrated-electron dynamics in the x-ray spectrum.

Radiolysis of liquid water is a universal phenomenon that accompanies the interaction of high-energy radiation with matter in aqueous environments. It is of fundamental importance in many domains (*1*), ranging from water-cooled nuclear reactors where radiolysis products cause corrosion (*2*) to radiation-induced genomic damage in living organisms where water comprises 80% by weight (*3*), thereby making radiolysis foundational to medical treatment, diagnosis and even extended human space flight (*4*). While ionizing radiation is delivered via various vehicles (x-rays, γ-rays, charged particles) its interaction with matter can be understood conceptually as individual absorption events along the particle path accompanied by a cascade of electrons, ions and radicals (*5*).

Consider the most elementary process: ionization of pure liquid water which leads to the

formation of a hydrated electron precursor and a cationic hole (H_2O^+). Both species are very reactive. The dynamics of the hydrated electron, e^-_{aq}, has been the subject of numerous studies (*6–11*) since the discovery of its visible spectrum (*12*), which peaks at 718 nm and spans 500-1000 nm - convenient for ultrafast laser spectroscopies. In stark contrast, its ionization partner, H_2O^+, has not been experimentally detected. The H_2O^+ is predicted to undergo rapid sub-100-fs proton transfer to a neighboring water molecule to yield the hydronium cation (H_3O^+) and the hydroxyl radical (OH) (*1, 14, 15*). Attempts to observe directly the H_2O^+ cation using ultrafast visible or ultraviolet probes have been inconclusive due to its ultrashort lifetime and masked spectral signature (*6, 13, 15*). Thus, basic questions regarding the ionization of water remain. What is the lifetime of H_2O^+? What are the absorption spectra of H_2O^+ and OH? What is the extent of hole delocalization in H_2O^+ and its timescale for localization relative to proton transfer?

Here we introduce an ultrafast x-ray probe which enables us to track the primary chemical reaction following ionization of liquid water, namely $H_2O^+ + H_2O \rightarrow OH + H_3O^+$. Combined experiment and theory yield insight for the effort in this new spectral regime. X-rays are well-suited for probing the short-lived H_2O^+ cation and OH radical as their absorption lines fall cleanly in the water window. Removal of an electron from the outermost valence orbital ($1b_1$) of H_2O produces a new transition for H_2O^+ that is red-shifted from the $1a_1 \rightarrow 4a_1$ pre-edge transition at 535 eV (*16*) roughly by the HOMO-LUMO gap ΔE (*17*), as shown in Fig. 1A. The OH radical, isoelectronic to H_2O^+, possesses a nearby x-ray absorption resonance, while the other product of proton transfer, H_3O^+, has resonances that fall in a region of strong water absorption (Fig. 1B). The experimental configuration, consisting of a 60-fs, 800-nm strong-field ionization pump (*10*), tunable $\sim$30 fs ultrafast x-ray probe from the LCLS (Linac Coherent Light Source) x-ray free-electron laser (XFEL) (*18*) and three photon-in/photon-out detection channels, is shown in Fig. 1C.

Signatures of the impulsively produced valence hole and excess electron appeared in all three detection channels when the incident x-ray energy was scanned. Fig. 2A displays data from the dispersed fluorescence channel, whereas the transmission mode is used in Figs. 2B, C and D. Fig. 2A shows absorption prior to ($\Delta t < 0$ ps) and after ionization ($\Delta t > 100$ fs). At negative time delay, the absorption is that of liquid water, i.e. nonresonant ionization of the valence and inner-valence levels of water plus the pre-edge transition. (Saturation effects prevented a clear observation of the pre-edge resonance.) At positive time delay, two new features are apparent: an absorption resonance at 525.9 eV and a shift of the pre-edge absorption to lower energies. The new absorption resonance is consistent with the creation of a hole in the outermost valence level of liquid water. The corresponding H_2O^+ transition energy can be estimated to be 526.9 eV using the binding energies in liquid water of the O 1s core level (538.1 eV) (*19*) and the $1b_1$ HOMO (11.2 eV) (*20*). The isoelectronic OH exhibits a gas-phase absorption peak at 525.85 eV (*21*).

The H_2O^+ cation produced by the ionization of liquid water is widely expected to decay via a pseudo-first-order reaction involving proton transfer to a neighboring water molecule

$$H_2O^+ + H_2O \rightarrow OH + H_3O^+ \tag{1}$$

to yield the OH radical and the H_3O^+ species. In the absence of electron scavengers, the OH radical subsequently undergoes geminate recombination (*22*) with the ejected electron to give OH^-. The time-resolved differential absorption spectrum, $\Delta A = A(\Delta t) - A(\Delta t < 0)$, showed a prompt increase at time-zero, followed by a narrowing of the spectral width within the first picosecond, and finally a gradual decay at longer time delays (Fig. 2B). We modeled this behavior as sequential kinetics: the species initially produced by ionization decays with lifetime τ_1 to give an intermediate species with lifetime τ_2, with absorption spectra $S_1(E)$ and $S_2(E)$, respectively.

We assign $S_2(E)$, obtained by averaging ΔA for time delays between $1.5-5.8$ ps, to the OH radical (Fig. 2C). $S_2(E)$ can be fit to a sum of two Lorentzians, a main peak at 525.97 ± 0.08 eV and a $\sim 7\times$ weaker sideband at 526.45 ± 0.12 eV. The 0.48-eV energy spacing between the two peaks is in reasonable agreement with the 0.53-eV spacing of the vibrational progression for core-excited gas-phase OH (*21*). Both peaks have a common FWHM (full width at half maximum) of 0.48 ± 0.02 eV, significantly broader than the 0.1-eV spectral bandwidth of the XFEL pulses and the 0.147-eV natural linewidth (*21*), suggesting inhomogeneous broadening by the solvent environment.

With the x-ray absorption lineshape of the aqueous OH radical $S_2(E)$ determined, the next step is to extract the time constants τ_1 and τ_2, and the spectral lineshape of the short-lived component $S_1(E)$. We used a Gaussian instrument response function of 106-fs FWHM and performed a surface fit of the experimental data shown in Fig. 2B. (We did not convolve the kinetic model with the experimental energy resolution of 0.1-eV FWHM because the experimentally observed spectral features were much broader.) The surface fit yielded $\tau_1 = 0.18 \pm 0.02$ ps and $\tau_2 = 14.2 \pm 0.4$ ps and a Lorentzian absorption lineshape $S_1(E)$ centered at 526.01 ± 0.13 eV with a FWHM of 0.98 ± 0.04 eV. The decay of the OH radical, τ_2, most likely originates from geminate recombination of the OH radical with a hydrated electron. The recombination time constant of 14.2 ± 0.4 ps is significantly shorter than those reported in the literature (*22*), most likely due to the high initial ionization fraction accelerating the geminate recombination process. Geminate recombination between e^-_{aq} and OH in ionized liquid water has been extensively investigated by time-resolved optical spectroscopy (*22*) and is beyond the scope of the present study. Nevertheless, considering the relative diffusion coefficients of the reactants and the reaction radius, our observed timescale for geminate recombination suggests an approximate ionization fraction of 1.7%, in relatively good agreement with the ionization fraction estimated based on the OH x-ray absorbance (see below). The spectral lineshape $S_1(E)$ and

time constant τ_1 can be assigned either to the decay of H_2O^+ or to the cooling of vibrationally hot OH radical. Both species should exhibit a larger spectral linewidth than the OH radical. The x-ray absorption linewidth of H_2O^+ may be similar to the 1.5-eV-wide $1b_1$ band in the valence photoelectron (*20*) and the x-ray emission spectra (*23*) of liquid water, whose widths have been attributed to a multitude of hydrogen-bonding configurations and intermolecular geometries. The x-ray absorption spectrum of vibrationally excited OH may be broadened due to the presence of additional hot-band transitions.

Further insight into the early-time dynamics was obtained with time traces at three selected photon energies: 525.43, 525.93, and 526.73 eV (Fig. 2D). These time traces correspond to the isotropic signal $\Delta A_{iso} = (\Delta A_{\parallel} + 2\Delta A_{\perp})/3$, reconstructed from measurements in which the relative polarizations of the pump and probe pulses are parallel ($\Delta A_{\parallel}$) and perpendicular ($\Delta A_{\perp}$). ΔA_{iso} is independent of rotational reorientation of the transient species in solution and is therefore sensitive only to population dynamics. Importantly, and visible upon inspection, the ΔA_{iso} time trace for 525.93 eV shows a significantly delayed rise relative to those for 525.43 and 526.73 eV. Attempts to perform a global fit with two time constants could not reproduce the early time dynamics (see SM, Supplementary Materials, for details). The presence of this delayed rise suggests the existence of an additional ultrafast process (*24*) that was not captured in our analysis of the 2D dataset shown in Fig. 2B. Indeed, global fitting of the ΔA_{iso} time traces revealed a new component with the time constant 46 ± 10 fs, whereas the other two time constants extracted from the fit, 0.16 ± 0.03 ps, and 9.2 ± 1.3 ps, are comparable to those obtained from the analysis of the 2D dataset. This additional time constant appeared as a growth component at 525.93 eV and to a smaller extent, at 526.73 eV as well, hence accounting for their delayed appearances relative to the signal at 525.43 eV, which rose with the instrument response function where prompt absorption by vertically ionized water might be expected based upon the calculated relative positions of the OH and H_2O^+ resonances. That the

46-fs component manifested itself as a growing signal at 525.93 eV, near the peak position of the OH radical absorption maximum at 525.97 eV, strongly suggests that it reflects the timescale for the formation of the OH radical. Given that OH is formed from the decay of the H_2O^+ radical cation, this interpretation would therefore suggest a lifetime of 46 fs for the H_2O^+ radical cation. The experiments were conducted at near-ambient temperature making them practically relevant. In this non-equilibrium situation, any local temperature rise does not affect the ultrafast proton transfer timescale.

To understand the observed ultrafast dynamics, we performed QM/MM excited-state molecular dynamics simulations of liquid water following strong-field ionization. We considered initial ionization in the upper 1.5 eV of the valence band and averaged across 107 initial geometries of liquid water. Non-Born-Oppenheimer effects were taken into account by Tully's fewest-switches surface hopping approach (*25*). We combined a quantum-mechanical (QM) description of a $(H_2O)_{12}^+$ cluster with a classical (MM) description of surrounding water molecules. The electronic structure was obtained at the Hartree-Fock level of theory employing Koopmans' theorem to obtain singly-ionized states and using the 6-31G basis set as implemented in our software package XMOLECULE (*26, 27*). (See SM for details).

Our simulations explored to what extent transient x-ray absorption is sensitive to ultrafast structural dynamics in water. The time-resolved x-ray absorption spectrum of the valence hole is shown in Fig. 3A for up to 100 fs after the initial hole formation. While initially electronic states down to HOMO-6 were populated, the trajectories arrived at the cationic ground state within 25 fs (Fig. 3B), and non-Born-Oppenheimer effects were no longer present. This was accompanied by hole localization on a comparable timescale.

Proton transfer can be characterized by the distance between the charge and hole center. Directly after ionization, the charge and hole are overlapped at the H_2O^+; as proton transfer proceeds, the hole stays on the OH moiety, while the charge is carried away by the H_3O^+ (*15*).

Fig. 3C shows that the charge-hole separation is correlated with the completion of the proton transfer. Within our model using bond order analysis (*28*), the proton transfer timescale was found to be 60 fs, in good agreement with Ref. (*15*). We further investigated the chemical environment surrounding the H_2O^+/OH, where the valence hole is located, to extract correlations with x-ray spectral signatures. The average distance of the H_2O^+/OH-oxygen to the nearest H_2O-oxygen is shown in Fig. 3D along with the spectral shift (the peak position of Fig. 3A). Initially, the partially negatively charged oxygens are pulled towards the region of positive charge (H_2O^+), giving rise to the redshift of the absorption peak. Note that this motion initiates proton transfer, and thus at the point of maximum redshift, proton transfer is only about 25% complete (Fig. 3C). As a consequence of charge-hole separation, the distance between OH and the neighboring oxygens increases, and the redshift shrinks. In this way, proton transfer is indirectly reflected in the time evolution of the x-ray absorption peak position.

The results presented here offer new insight into the elementary dynamics of the highly reactive and short-lived ion and neutral radical species in ionized liquid water. Our experimental approach offers several advantages compared to previous attempts (*6, 13, 15*) to determine the lifetime of the elusive H_2O^+ radical cation. First, compared to traditional two-photon UV photoionization, strong-field ionization provides access to a large concentration of ionized species in solution. Assuming a cross section of $\sim$7 Mbarn for the O 1s resonant absorption of the OH radical, we estimated an ionization fraction of $\sim 0.8\%$ under our experimental conditions. Second, the H_2O^+ and OH radicals exhibit strong O $1s \rightarrow 2p$-like resonant transitions in the soft x-ray absorption spectra because they possess open O 2p sub-shells. These resonances occur in the background-free, near-edge spectral region, enabling detection down to few millimolar concentration. In comparison, previous attempts by spectrally resolved visible transient absorption spectroscopy to observe the H_2O^+ radical cation via its predicted absorption signature at 2.3 eV were unsuccessful due to its weak absorption being masked by the strong, broad hydrated elec-

tron absorption feature, and, further complicated by cross-phase modulation artifacts (*6, 13, 15*).

The present study revealed three distinct timescales in the early-time dynamics of ionized liquid water: 46 ± 10 fs, 0.18 ± 0.02 ps, and 14.2 ± 0.4 ps, tentatively assigned to the decay of the H_2O^+ radical cation via proton transfer, vibrational cooling of the hot OH radical produced from H_2O^+, and geminate recombination of OH with the hydrated electron byproduct, respectively. The first two processes, hitherto unobserved, are of particular interest. The assignment of the 46-fs component to the lifetime of the H_2O^+ cation is supported by QM/MM molecular dynamics simulations, which predict a lifetime of 60 fs. However, we note that the same simulations also showed that hole localization occurs within 30 fs. As such, with the presently available time resolution, hole localization also contributed to the observed dynamics. On the intermediate timescale, the 0.18-ps component was tentatively assigned to vibrational cooling of hot OH radicals, produced upon ultrafast proton transfer. The formation of a vibrationally excited OH product from H_2O^+ is likely considering the 3% change in equilibrium OH bond lengths between gas-phase H_2O^+ (0.9992Å) (*29*) and OH (0.9697Å) (*30*). The assignment of the 0.18-ps component to vibrational relaxation of the OH radical is supported by studies of the OH stretch of liquid H_2O where numerous time-resolved infrared spectroscopic measurements show vibrational relaxation and vibrational energy transfer occurring within 0.2 - 0.3 ps (*31, 32*).

We expect that a future study with higher time resolution and signal-to-noise ratios could furnish a more accurate H_2O^+ lifetime and at the same time, permit the observation of ultrafast dynamics involving possible hole alignment, coherences and non-adiabatic dynamics induced by radiolysis. With improved statistics over a wide range of probe photon energies, we also anticipate the possibility of isolating the spectral signatures of H_2O^+ and the hot OH radical. Interestingly, in addition to valence hole dynamics observed at 526 eV, the soft x-ray probe appeared to be sensitive to the dynamics of the electron that was injected into the solvent by ionization. The spectral changes observed in the vicinity of the pre-edge absorption (531.0

- 533.7 eV) fit a universal time constant of 0.26 ± 0.03 ps that matches previous studies of hydrated electron formation (*7, 8*) (See SM). Future experiments focusing on the pre- and main-edges of ionized liquid water which require a sub-micrometer-thick liquid jet could potentially yield the electronic energy level diagram of ionized liquid water (*33*) and shed light on its electronic relaxation dynamics, as well as possibly discern the cavity vs. non-cavity model for the structure of the hydrated electron (*34*).

References

1. B.C. Garrett *et al.*, *Chem. Rev.* **105**, 355-389 (2005).

2. S. Gordon in *Early Developments in Radiation Chemistry*, edited by J. Kroh (Royal Society of Chemistry (1989)) pp 163.

3. E. Alizadeh, L. Sanche, *Chem. Rev.* **112**, 5578-5602 (2012).

4. F.E. Garrett-Bakelman *et al.*, *Science* **364**, 144 (2019).

5. M. Inokuti, *Rev. Mod. Phys.* **43**, 297-347 (1971).

6. F. H. Long, H. Lu, K. B. Eisenthal, *Phys. Rev. Lett.* **64**, 1469-1472 (1990).

7. A. Migus, Y. Gauduel, J. L. Martin, A. Antonetti, *Phys. Rev. Lett.* **58**, 1559-1562 (1987).

8. P. Kambhampati, D.H. Son, T.W. Kee, P.F. Barbara, *J. Phys. Chem. A* **106**, 2374-2378 (2002).

9. M.H. Elkins, H.L. Williams, A.T. Shreve, D.M. Neumark, *Science* **342**, 1496-1499 (2013).

10. J. Li, Z. Nie, Y.Y. Zheng, S. Dong, Z.-H. Loh, *J. Phys. Chem. Lett* **4**, 3698-3703 (2013).

11. J.M. Herbert, M.P. Coons, *Annu. Rev. Phys. Chem* **68**, 447-472 (2017).

12. E. J. Hart, J.W. Boag, *J. Am. Chem. Soc.* **84**, 4090-4095 (1962).

13. Y. Gauduel, S. Pommeret, A. Migus, A. Antonetti, *Chem. Phys.* **149**, 1-10 (1990).

14. E. Kamarchik, O. Kostko, J.M. Bowman, M. Ahmed, A.I. Krylov, *J. Chem. Phys.* **132**, 194311 (2010).

15. O. Marsalek *et al.*, *J. Chem. Phys.* **135**, 224510 (2011).

16. Th. Fransson *et al.*, *Chem. Rev.* **116**, 7551-7569 (2016).

17. C. Elles *et al.*, *J. Chem. Phys* **130**, 084501- (2009).

18. P. Emma *et al.*, *Nat. Photon.* **4**, 641-647 (2010).

19. B. Winter, E.F. Aziz, U. Hergenhahn, M. Faubel, I.V. Hertel, *J. Chem. Phys.* **126**, 124504 (2007).

20. K. Nishizawa *et al.*, *Phys. Chem. Chem. Phys.*, **13**, 413417 (2011).

21. S. Stranges, R. Richter, M. Alagia, *J. Chem. Phys.* **116**, 3676-3680 (2002).

22. R.A. Crowell, D.M. Bartels, *J. Phys. Chem.* **100**, 17940-17949 (1996).

23. J.H. Guo *et al.*, *Phys. Rev. Lett.* **89**, 137402 (2002).

24. M.J. Rosker, M. Dantus, A.H. Zewail, *J. Chem. Phys.* **89**, 6113-6127 (1988).

25. J.C. Tully, *J. Chem. Phys.* **93**, 1061-1071 (1990).

26. Y. Hao, L. Inhester, K. Hanasaki, S.-K. Son, R. Santra, *Struct. Dyn.* **2**, 041707 (2015).

27. K. Khalili, L. Inhester, C. Arnold, R. Welsch, J. W. Andreasen, R. Santra, *Struct. Dyn.* **6**, 044102 (2019).

28. L. Inhester *et al.*, *J. Phys. Chem. Lett.* **9**, 1156-1163 (2018).

29. T.R. Huet, C.J. Pursell, W.C. Ho, B.M. Dinelli, T. Oka, *J. Chem. Phys.* **97**, 5977-5987 (1992).

30. K.P. Huber, G. Herzberg in NIST Chemistry WebBook, NIST Standard Reference Database Number 69 (Eds P. J. Linstrom and W. G. Mallard) (National Institute of Standards and Technology) Available at http://webbook.nist.gov.

31. F. Perakis, L. De Marco, A. Shalit, F. Tang, Z. R. Kann, T.D. Khne, R. Torre, M. Bonn, Y. Nagata, *Chem. Rev.* **116**, 7590-7607 (2016).

32. M.L. Cowan, B.D. Bruner, N. Huse, J.R. Dwyer, B. Chugh, E.T.J. Nibbering, T. Elsaesser, R.J.D. Miller, *Nature* **434**, 199-202 (2005).

33. A.P. Gaiduk, T.A. Pham, M. Govoni, F. Paesani, G. Galli, *Nat. Commun.* **9**, 247 (2018).

34. R.E. Larsen, W.J. Glover, B.J. Schwartz, *Science* **329**, 65-69 (2010).

35. M.L. Vidal, X. Feng, E. Epifanovsky, A.I. Krylov, S. Coriani, *J. Chem. Theo. Comp.* **15**, 3117-3133 (2019).

36. M. Nagasaka, T. Hatsui, T. Horigome, Y. Hamamura, N. Kosugi, *J. Elec. Spec. Rel. Pheno.* **177**, 130-134 (2010).

37. L. Young, Z.-H. Loh, R. Santra, C. Arnold, Data for Observation of the fastest chemical processes in the radiolysis of water. Zenodo repository. DOI: 10.5281/zenodo.3543680

38. W. F. Schlotter *et al.*, *Rev. Sci. Instrum.* **83**, 043107 (2012).

39. J. Koralek *et al.*, *Nat. Commum.* **9**, 1353 (2019).

40. P. Heimann *et al.*, *Rev. Sci. Instrum.* **82**, 093104 (2011).

41. Y-D. Chuang *et al.*, *Rev. Sci. Instrum.* **88**, 013110 (2017).

42. D.J. Higley *et al.*, *Rev. Sci. Instrum.* **87**, 033110 (2016).

43. M. Beye *et al.*, *Appl. Phys. Lett.* **100**, 121108 (2012).

44. J. Niskanen, M. Fondella, C. J. Sahle, S. Eckert, R. M. Jay, K. Gilmore, A. Pietzsch, M. Dantze, X. Lue, D. E. McNally, T. Schmitt, V. Vaz da Cruz, V. Kimberg, F. Gel'mukhanov, and A. Föhlisch, *Proc. Nat. Acad. Sci.* **116**, 4058 - 4063 (2019).

45. K. Yamazoe, J. Miyawaki, H. Niwa, A. Nilsson, Y. Harada, Measurements of Ultrafast Dissociation in Resonant Inelastic X-ray Scattering of Water, *J. Chem. Phys.* **150**, 204201 (2019).

46. C.D. Cappa, J.D. Smith, B.M. Messer, R.C. Cohen, R.J. Saykally, *J. Phys. Chem. A* **111**, 4776-4785 (2007).

47. D. Prendergast, G. Galli, *Phys. Rev. Lett.* **96**, 215502 (2006).

48. H. Wen, N. Huse, R. W. Schoenlein, A. M. Lindenberg, *J. Chem. Phys.* **131**, 234505 (2009).

49. F. Maseras and K. Morokuma, *J. Comp. Chem.* **16**, 11701179, (1995).

50. P. Mark and L. Nilsson, *J. Phys. Chem. A* **105**, 9954-9960 (2001).

51. H.C. Andersen, *J. Comp. Phys.* **52**, 24-34 (1983).

Acknowledgments

Funding: This work was supported by the U.S. Department of Energy, Office of Science, Basic Energy Science, Chemical Sciences, Geosciences and Biosciences Division who supported

the Argonne group under contract number DE-AC02-06CH11357. Use of the Linac Coherent Light Source (LCLS), SLAC National Accelerator Laboratory, and, resources of the Center for Nanoscale Materials (CNM), Argonne National Laboratory, are supported by the U.S. Department of Energy (DOE), Office of Science, Office of Basic Energy Sciences (BES) under Contracts DE-AC02-76SF00515 and DE-AC02-06CH11357. L.Y. acknowledges support from Laboratory Directed Research and Development (LDRD) funding from Argonne National Laboratory for conceptual design and proposal preparation. Z.-H.L., T.D., and M.S.B.M.Y. acknowledge support from the Singapore Ministry of Education (MOE2014-T2-2-052 and RG105/17). L.K., J.-E.R. acknowledge support from the Swedish Science Council (2018-04088). M.S. was supported by the CNRS GotoXFEL program. C.A., R.W., and R.S. were supported by the Cluster of Excellence 'Advanced Imaging of Matter' of the Deutsche Forschungsgemeinschaft (DFG) - EXC 2056 - project ID 390715994. L.I. and R.S. acknowledge support by the Chemical Sciences, Geosciences, and Biosciences Division, Office of Basic Energy Sciences, Office of Science, U.S. Department of Energy, Grant No. DE-SC0019451. K.K. was supported by the European Research Council (ERC) under the European Union's Horizon 2020 research and innovation programme (Grant Agreement No. 681881). A.I.K. and K.N. were supported by the U.S. National Science Foundation (No. CHE-1856342). A.I.K. is also a grateful recipient of the Simons Fellowship in Theoretical Physics and Mildred Dresselhaus Award from the Hamburg Centre for Ultrafast Imaging, which supported her sabbatical stay in Germany. **Author contributions:** L.Y., Z.-H.L. and R.S. originated the project concept. W.F.S., G.D., M.-F.T., R.D.S. and S.H.S. designed the experimental apparatus and characterized the target. Z.-H.L., G.D., C.A., L.K., S.H.S., A.A.H., Y.K., M.-F.T., P.J.H., A.M.M., M.S.B.M.Y., T.D. M.S., S.M, G.C., J.K., M.P.M., W.F.S., J.-E.R., and L.Y. executed the experiment and collected the experimental data. Z.-H.L., Y.K., L.K., J.-E.R. and L.Y. analyzed the experimental data. R.S., C.A., R.W., L.I, K.K., K.N. and A.K. provided supporting theoretical calculations. L.Y., Z.-H.L., R.S. and

C.A. wrote the paper with comments from all authors. L.Y. was responsible for the coordination of the project. **Competing interests:** A.I.K. is a board member and a part-time owner of Q-Chem. Inc.. **Data and materials availability:** The underlying data are available in the supplementary materials and Zenodo, the CERN repository (*37*).

Supplementary materials

Materials and Methods

Supplementary Text

Figs. S1 to S11

Tables S1 to S3

References *(38-51)*

Fig. 1. Ultrafast x-ray laser probe of ionization dynamics of liquid water. **(A)** Ionization of H_2O produces H_2O^+ with a strong isolated soft x-ray absorption resonance ($1a_1 \rightarrow 1b_1$). **(B)** Absorption resonances in the gas phase for the four species associated with elementary proton transfer: H_2O^+ + $H_2O \rightarrow$ OH + H_3O^+ calculated with 6-311(2+,+)G(2df,p) basis with uncontracted core (oxygen) using fc-cvs-EOM-CCSD (*35*). Only H_2O^+ and OH fall outside the region of strong absorption by liquid water (*36*), i.e. in the water window. **(C)** Schematic of the experimental setup: 800-nm strong-field ionization pump and time-delayed x-ray probe. The x-ray probe is monitored simultaneously in transmission, total fluorescence and dispersed fluorescence as a function of pump-probe time delay and incident photon energy. See Materials and Methods.

Fig. 2. Transient x-ray absorption spectroscopy for the reaction H_2O^+ + $H_2O \rightarrow$ OH + H_3O^+. **(A)** Absorption for $\Delta t < 0$ and $\Delta t > 100$ fs monitored through the dispersed fluorescence channel. **(B)** Differential absorption ΔA in the valence hole (H_2O^+/OH) region. Spectra collected at 216 time delays between 1.5 5.8 ps are averaged to produce the resonance profile, which is fit to a sum of two Lorentzians. Error bars correspond to the standard deviation. A total of 31 energy sweeps and 27546 shots are collected. **(C)** X-ray absorption spectrum of the aqueous OH radical. **(D)** Polarization averaged time traces at three x-ray probe energies, 525.43, 525.93 and 526.73 eV.

Fig. 3. Calculated x-ray absorption spectra and trajectory analysis. **(A)** Resonant x-ray absorption spectrum of ionized water. **(B)** Hole radius (green) and non-adiabatic dynamics (gray, solid line shows average). **(C)** Charge–hole distance (CHD) (blue) and completed proton transfer percentage (orange). **(D)** Average distance between oxygens in H_2O molecules (black) along with the average distance of the H_2O^+/OH oxygen to the nearest oxygen (purple) and the spectral shift of the x-ray absorption resonance (red).

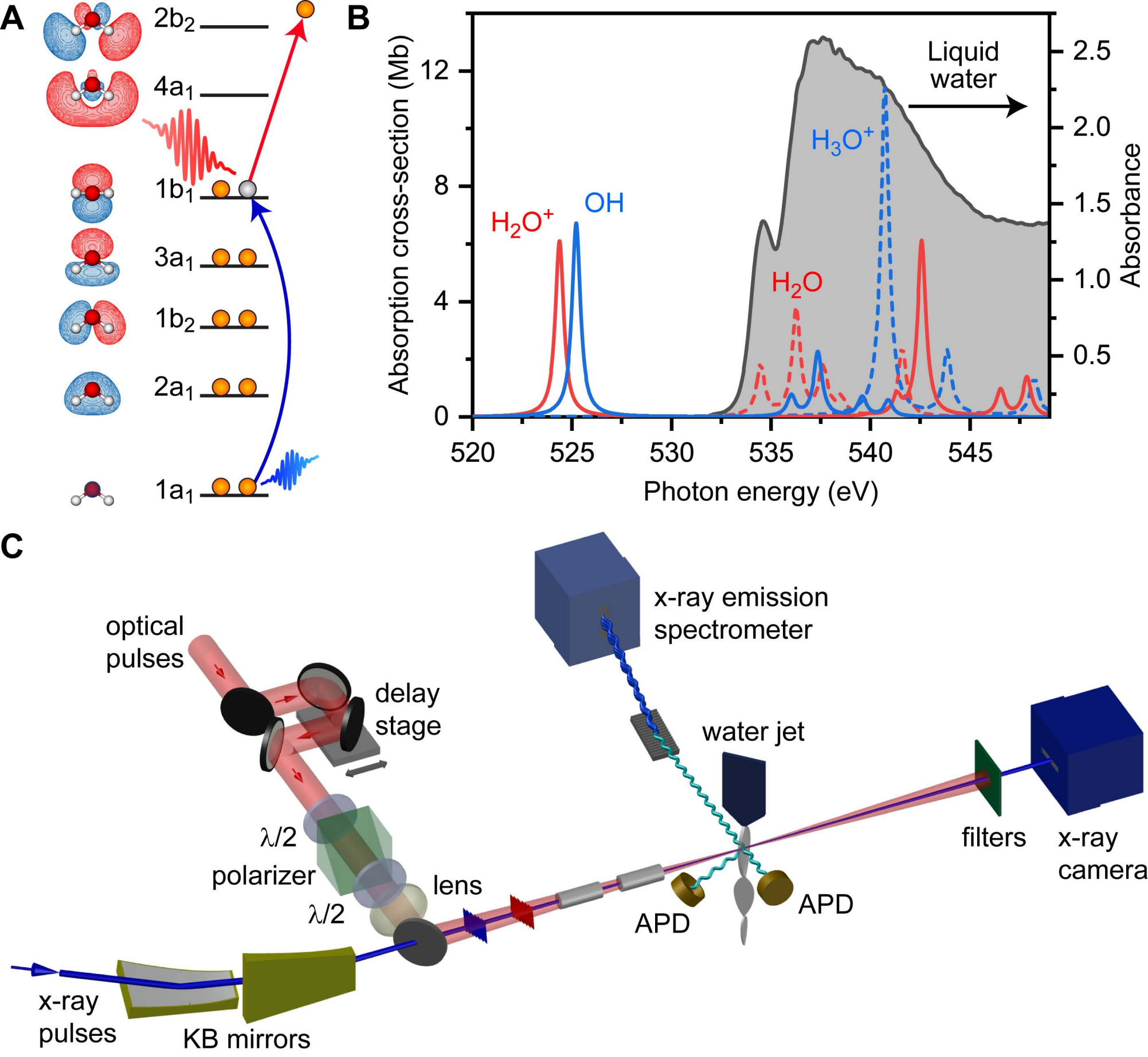
A
2b2
4a1
1b1
3a1
1b2
2a1
1a1
B
Absorption cross-section (Mb)
Absorbance
Photon energy (eV)
Liquid water
H3O+
OH
H2O+
H2O
C
optical pulses
delay stage
λ/2
polarizer
λ/2
lens
x-ray pulses
KB mirrors
x-ray emission spectrometer
water jet
APD
APD
filters
x-ray camera

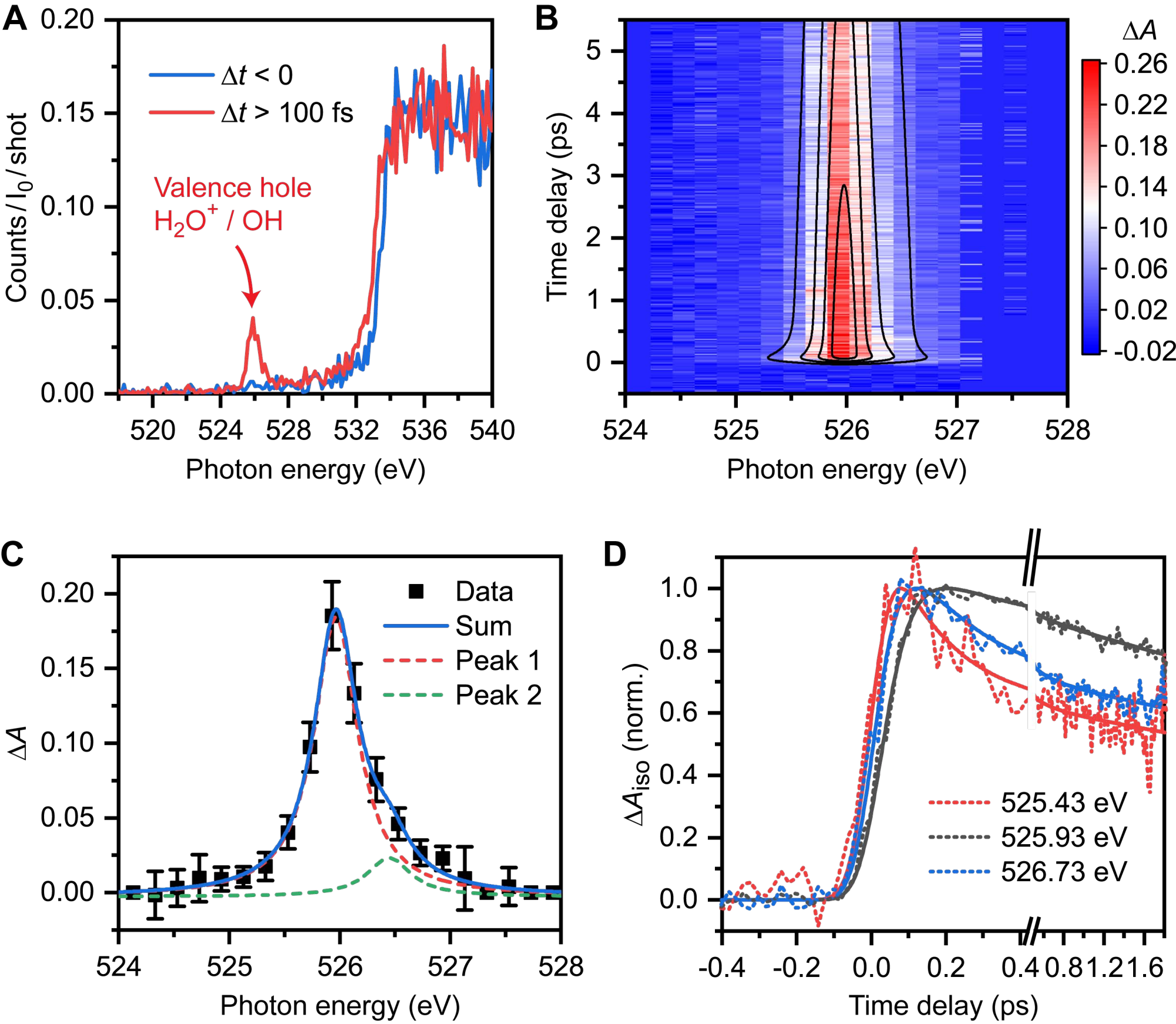
A
B
C
D
Counts / I0 / shot
Δt < 0
Δt > 100 fs
Valence hole
H2O+ / OH
Photon energy (eV)
Time delay (ps)
ΔA
Data
Sum
Peak 1
Peak 2
ΔAiso (norm.)
525.43 eV
525.93 eV
526.73 eV

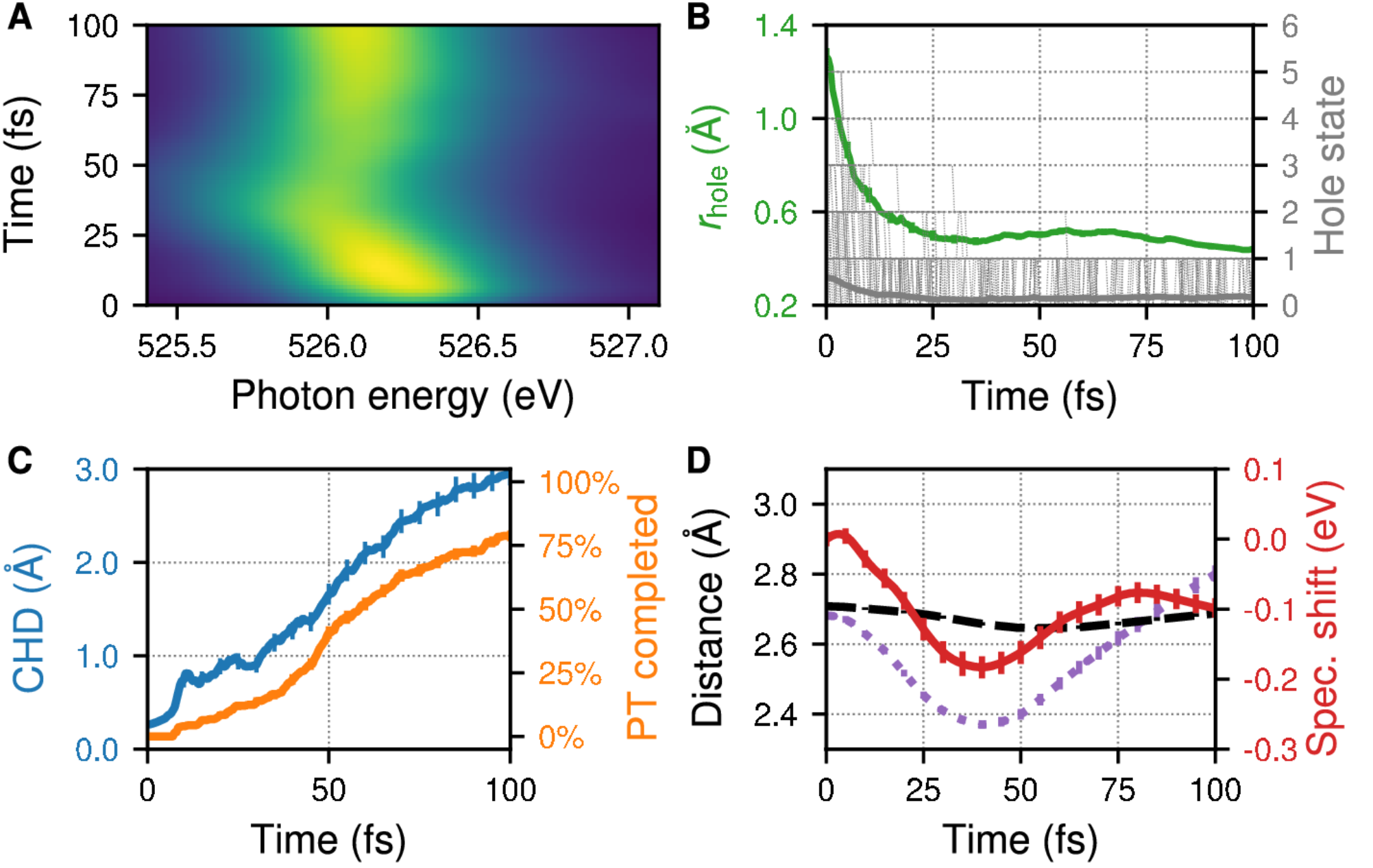
A
Time (fs)
100
75
50
25
0
525.5
526.0
526.5
527.0
Photon energy (eV)
B
1.4
1.0
0.6
0.2
r_{hole} (Å)
6
5
4
3
2
1
0
Hole state
0
25
50
75
100
Time (fs)
C
3.0
2.0
1.0
0.0
CHD (Å)
100%
75%
50%
25%
0%
PT completed
0
50
100
Time (fs)
D
3.0
2.8
2.6
2.4
Distance (Å)
0.1
0.0
-0.1
-0.2
-0.3
Spec. shift (eV)
0
25
50
75
100
Time (fs)

Supplementary Information: Observation of the fastest chemical processes in the radiolysis of water

Z.-H. Loh,[1*] G. Doumy,[2] C. Arnold,[3,4,5] L. Kjellsson,[6,7] S.H. Southworth,[2]
A. Al Haddad,[2] Y. Kumagai,[2] M.-F. Tu,[2] P.J. Ho,[2], A.M. March,[2]
R.D. Schaller,[8,9] M.S. Bin Mohd Yusof,[1] T. Debnath,[1] M. Simon,[10]
R. Welsch,[3,5] L. Inhester,[3] K. Khalili,[11] K. Nanda,[12] A.I. Krylov,[12]
S. Moeller,[13] G. Coslovich,[13] J. Koralek,[13] M.P. Minitti,[13] W.F. Schlotter,[13]
J.-E. Rubensson,[6], R. Santra,[3,4,5*] L. Young[2,14*]

[1]Division of Chemistry and Biological Chemistry, School of Physical and Mathematical Sciences,
Nanyang Technological University, Singapore
[2]Chemical Sciences and Engineering Division, Argonne National Laboratory, Lemont, IL USA
[3]Center for Free-Electron Laser Science, DESY, Hamburg, Germany
[4]Department of Physics, Universität Hamburg, Hamburg, Germany
[5]The Hamburg Centre for Ultrafast Imaging, Hamburg, Germany
[6]Department of Physics and Astronomy, Uppsala University, Uppsala, Sweden
[7]European XFEL GmbH, Schenefeld, Germany
[9]Center for Nanoscale Materials, Argonne National Laboratory, Lemont, IL, USA
[10]Department of Chemistry, Northwestern University, Evanston, IL, USA
[11]Sorbonne Université and CNRS, Laboratoire de
Chemie Physique-Matière et Rayonnement, LCPMR, F-750005, Paris, France
[12]Department of Energy Conversion and Storage,
Technical University of Denmark, Roskilde, Denmark
[13]Department of Chemistry, University of Southern California, Los Angeles, CA, USA
[14]LCLS, SLAC National Accelerator Laboratory, Menlo Park, CA, USA
[15]Department of Physics and James Franck Institute, The University of Chicago, Chicago, IL, USA

[*]To whom correspondence should be addressed;
E-mail: zhiheng@ntu.edu.sg, robin.santra@cfel.de, young@anl.gov

1 Methods and Materials

The optical ionization pump-soft x-ray probe measurements were performed at the soft x-ray (SXR) endstation (*38*) of the Linac Coherent Light Source (LCLS) x-ray free-electron laser (XFEL). The 800-nm output of a Ti:sapphire amplifier is focused onto a 2-μm-thick colliding liquid sheet jet target (*39*) to ionize liquid water by strong-field ionization. The surface of the liquid jet is oriented at 45° relative to the incident 800-nm ionization pump and soft x-ray probe beams, with a crossing angle of $\sim$1° between the two beams. With a pulse energy of 1.1 mJ, a focal spot size (1/e^2 diameter) of 170 (h) $\times$ 120 (v) μm^2, and a pulse duration of 60 fs, the peak intensity of the ionization pump pulse is 2.3×10^{14} W/cm^2, approximately one order of magnitude higher than that used in an earlier study of strong-field-ionized liquid water by ultrafast optical spectroscopy (*10*). The 20-fs XFEL pulse (40 fs for the survey scan shown in Fig. 2A), is monochromatized to a spectral width of 0.1 eV. This process also stretches the 20-fs pulse (*40*) to $\sim$30 fs. The monochromatized XFEL pulse is then focused by a pair of Kirkpatrick-Baez mirrors to a focal spot size (1/e^2 diameter) of 108 (h) $\times$ 17 (v) μm^2 on the ionized water target. The intensity and polarization of the 800-nm pump laser can be controlled by a $\lambda/2$, polarizer, $\lambda/2$ combination in the 800-nm delivery path.

Three different observables are recorded simultaneously in the experiments as shown in Fig. S1. The transmitted x-ray pulse energy is recorded by an x-ray CCD (upper panel); the spectrally-integrated x-ray fluorescence is monitored by a pair of silicon avalanche photodiodes (3-mm diameter, SAR3000G1 Laser Components) placed $\sim$3.2 cm from the target for a solid angle of 5.5×10^{-4} (middle panel); and the spectrally-resolved x-ray fluorescence is recorded by an x-ray emission spectrometer, with a collection/transmission efficiency of $\sim 10^{-7}$ (*41*) (lower panel). The transmission channel has the superior signal-to-noise ratio and was used for the kinetics analyses.

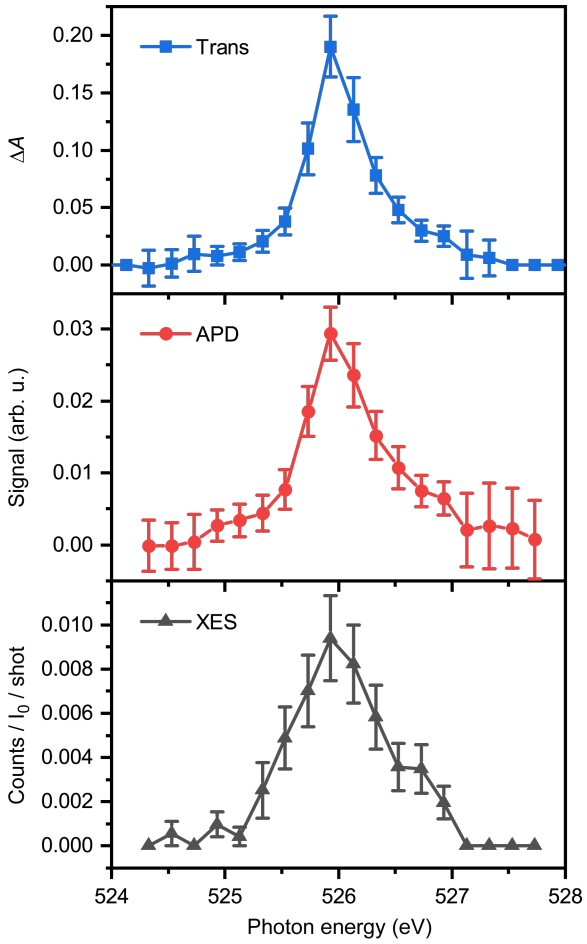

Figure S1: Simultaneous detection channels for x-ray transient absorption. Survey scan from 524-528 eV with 0.1-eV bandwidth, ∼30-fs pulses averaged over delay times 1-6 ps. A total of 31,181 out of 158,680 shots met the joint criteria for linear detector response to FEL intensity, acceptable time jitter, and laser power. Upper panel: transmission channel (differential absorption). Middle panel: APD signal (total fluorescence yield). Lower panel: dispersed emission (partial fluorescence yield). There are 24 counts at the maximum, a total of 130 counts and error bars are statistical.

Upstream of the liquid-jet endstation, a gas detector records the pulse energy of every XFEL pulse in the front-end enclosure for single-shot referencing and rejection of spurious pulses and a monochromator scans the incident x-ray photon energy in the range of 518 - 538 eV. The incident fluence monitor, I_0, of the monochromatized x-ray beam was checked for linearity with

respect to the upstream gas monitor; higher energy pulses in the nonlinear region were rejected from the transmission data analysis (*42*). An arrival time monitor positioned in the upstream Hutch 1 endstation monitors the relative arrival times of the optical laser and the XFEL pulses. In these experiments, the optical-XFEL timing jitter limits the effective time resolution to $\sim$110 fs (*43*).

The monochromator energy calibration (shift and dispersion) was determined as follows. The energy shift relative to the monochromator readout was determined by comparing the observed rise of the pre-edge absorption in our 2-μm water jet with that in a 800-nm water jet by Nagasaka *et al.* (*36*). The thickness of our colliding water jet at a flow rate of 3.5 ml/min (linear flow rate $\approx$ 40m/s) was measured using white light interference fringes to be $2.09 \pm 0.10\mu$m at the Center for Nanoscale Materials at Argonne National Laboratory. This value was used to determine the thickness of the jet in the experimental configuration, i.e. at 45° incidence angle, and to scale the absorbance values of Ref. (*36*). Using jet-on/jet-off data for 5 separate runs, we determined an energy shift relative to the monochromator readout of -2.07 ± 0.07 eV using the inflection of the pre-edge resonance as a reference point. The dispersion of the monochromator was checked with two reference points, the pre-edge feature as described above and the water XES emission doublet from the $1b_1$ orbital collected in the dispersed fluorescence channel for incident energies between 536 - 538 eV (*44*). In a single scan from 518 - 538 eV, we observe both reference points. The RIXS spectrum of the OH radical appears at the OH resonance energy (526 eV) and its elastic peak coincides with the lower energy partner of the water XES doublet. We find that the calibrated dispersion of the monochromator does not introduce an error larger than 0.07 eV (better than 1%) and use it directly. (We note that by using an alternative reported position for the XES emission doublet (*45*) would increase the monochromator dispersion by 5%, and shift the OH radical resonance by -0.4 eV.)

2 Intensity Dependence

Measurements were performed to investigate the dependence of the early-time dynamics on the intensity of the strong-field ionization pump pulse. In these measurements, the pump power was varied by using a combination of a half-wave plate and a linear polarizer while keeping the pulse duration and focal spot sizes fixed. The differential absorption signal at 525.93 eV, near the peak of the OH radical absorption, was recorded as a function of time delay for various fractions of the full pump intensity (2.3×10^{14} W/cm^2). All the time traces can be fit to a rise time of 49 ± 7 fs (Fig. S2), consistent with the time constant of 46 ± 10 fs obtained from the global analysis of the time traces shown in Fig. 2D of the main text. The absence of any intensity dependence suggests that the observed dynamics arise from the chemical dynamics of ionized liquid water rather than the collective, macroscopic dynamics of a plasma generated by strong-field ionization. It is noteworthy that the ΔA value in the positive-time region is only 0.007 for the lowest peak intensity (9.5×10^{13} W/cm^2) employed in the intensity-dependent measurements.

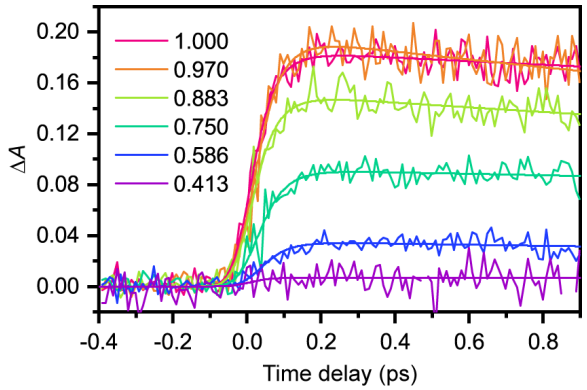

Figure S2: Intensity dependence of early time kinetics at different fractions of the full pump intensity. Differential absorption traces for an incident photon energy of 526 eV.

3 Sequential Kinetics Modeling

Surface Fit (Fig. 2B) A sequential kinetics model is used to fit the time-resolved ΔA spectrum taken in the 2D survey scan shown in Figure 2B. The model assumes that the species initially produced by ionization decays with lifetime τ_1 to give an intermediate species with lifetime τ_2, and that the absorption spectrum associated with each species is $S_1(E)$ and $S_2(E)$, where E is the probe photon energy. Within this framework, the ΔA signal as a function of time delay τ and E is given by the expression

$$\Delta A(E,t) = \left[S_1(E)e^{-t/\tau_1} + \frac{S_2(E)\tau_2}{\tau_2 - \tau_1}(e^{-t/\tau_2} - e^{-t/\tau_1}) \right] H(t) * IRF(t) \tag{S1}$$

where $H(t)$ is the Heaviside function. In our analysis we assume that $\tau_1 \ll 1$ ps, as suggested by the observed rapid narrowing of the ΔA spectrum on the sub-picosecond timescale, hence allowing the absorption lineshape $S_2(E)$ to be obtained by averaging the differential absorption spectra collected at pump-probe time delays > 1.5 ps.

Global Fit (Fig. 2D) Fig. 2D shows a clearly delayed appearance of the isotropic ΔA signal at 525.93 eV relative to 525.43 and 526.73 eV. The improved signal-to-noise ratio relative to the 2D data in Fig. 2B is due to a 10-fold increase in the number of shots per time bin.

The three time traces, prior to normalization, are fit to the function

$$\Delta A(t) = IRF(t) * H(t) \sum_{i=1}^{n} A_i e^{-t/\tau_i} \tag{S2}$$

where n specifies the number of exponential components, each with amplitude A_i and time constant τ_i. Each component is multiplied with the Heaviside function $H(t)$ before the product is convolved with the instrument response function $IRF(t)$. The full-width at half-maximum (FWHM) of $IRF(t)$, the time-zero value (t_0), and the time constants are set as shared parameters in the global fit.

In the spirit of the surface fit, we first attempted a fit to two time constants, with fixed t_0 and IRF. We find that it cannot reproduce the observed ordering of the delayed rise, which experimentally is 525.43 eV $<$ 526.73 eV $<$ 525.93 eV as displayed in Fig. S3. That is, the red-shifted trace rises first, followed by the blue-shifted trace and finally by the central trace (black). The best fit, however, shows the blue trace to rise first, rather than the red trace.

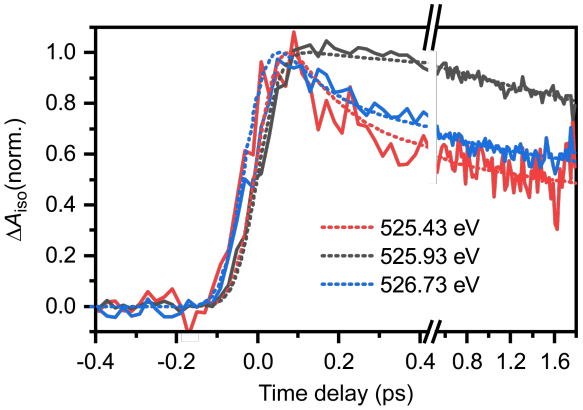

Figure S3: ΔA_{iso} traces (same as Fig 2D main text) for three different incident photon energies shown with the best fit using two-time constants.

Next we allowed the width of the instrument response function and the time-zero position to vary across the three probe photon energies while globally fitting the time traces to only two decay components. The resultant time-zero shifts (t_0) and full-width at half-maxima (FWHM) of the instrument response functions are summarized in Table S2 along with the time constants and amplitudes.

It is evident that significant deviations in the t_0 and FWHM values are needed to fit the time traces. In particular, in order to reproduce the pronounced delay in the rise of the signal at 525.93 eV, the FWHM value of the instrument response has to increase by 20% and the time-zero position shifts towards positive time by 44 fs. In addition to these significant changes in the t_0 and FWHM values, we also note the non-monotonic trend in the Δt_0 values as a function of X-ray photon energy. These observations are unrealistic, given that the monochromator is

Table S1: Parameters obtained from fitting the time traces in Figure S4 to independent $IRF(t)$, FWHM and time-zero values.

	525.43 eV	525.93 eV	526.73 eV
A_1	0.0174 $\pm$0.0036	0.0286 $\pm$0.0052	0.0367 $\pm$0.0042
A_2	0.0249$\pm$0.0014	0.2295$\pm$0.0054	0.0613$\pm$0.0020
τ_1(ps)		0.19 ± 0.03	
τ_2(ps)		8.2 ± 1.1	
Δt_0	-23 $\pm$57	44 $\pm$24	19 $\pm$33
FWHM(fs)	113 ± 24	142$\pm$4	133$\pm$12

tuned by only -0.5 and $+0.8$ eV from a central energy of 525.93 eV.

The addition of a third time component allows us to fit the early time dynamics as shown in Fig. S4 using the values summarized in Table S2

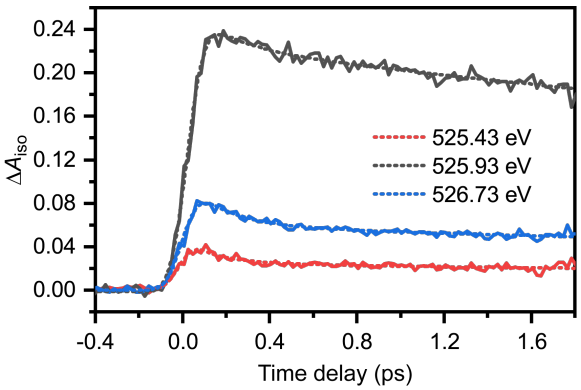

Figure S4: Unnormalized ΔA_{iso} traces (same as Fig 2D main text) for three different incident photon energies. The fit to a three exponential component function is also shown.

The new 46-fs component (A_3) is, within experimental error, absent at 525.43 eV, whereas it manifests itself as a rising signal at 525.93 eV ($A_3 < 0$) and to a smaller extent at 526.73 eV. The presence of the rising component accounts for the delayed appearance of the signal at 525.93 and 526.73 eV relative to 525.43 eV. Both the 0.16-ps and 9.2-ps components appear as a decaying signal across all three probe photon energies.

Table S2: Parameters obtained from fitting the time traces in Figure S4 to Eq. S2

	525.43 eV	525.93 eV	526.73 eV
A_1	0.0238±0.0076	0.0670±0.0270	0.0569±0.0162
A_2	0.0242±0.0012	0.2270±0.0053	0.0597 ±0.0018
A_3	0.0008±0.0152	-0.2907±0.0268	-0.0623±0.0231
τ_1(ps)		0.16 ± 0.03	
τ_2(ps)		9.2 ± 1.3	
τ_3(fs)		46 ± 10	
t_0		0	
FWHM (fs)		119 ± 7	

The presence of three time constants leads us to consider sequential kinetics involving four species

$$\mathrm{A} \xrightarrow{k_A} \mathrm{B} \xrightarrow{k_B} \mathrm{C} \xrightarrow{k_C} \mathrm{D} \tag{S3}$$

with rate constants k_A, k_B, and k_C. From the main text, A, B, C, and D correspond to H_2O^+, the vibrationally excited OH radical (OH^*), the OH radical in the vibrational ground state, and the OH^- anion. The time-dependent populations of these species are given by

$$N_A(t) = N_0 e^{-k_A t} \tag{S4}$$

$$N_B(t) = \frac{N_0 k_A}{k_B - k_A}\left(e^{-k_A t} - e^{-k_B t}\right) \tag{S5}$$

$$N_C(t) = \frac{N_0 k_A k_B}{k_B - k_A}\left[\frac{1}{k_C - k_A}\left(e^{-k_A t} - e^{-k_C t}\right) - \frac{1}{k_C - k_B}\left(e^{-k_B t} - e^{-k_C t}\right)\right] \tag{S6}$$

$$\begin{aligned} N_D(t) = N_0 - \frac{N_0 k_B k_C}{(k_A - k_B)(k_A - k_C)} e^{-k_A t} - \frac{N_0 k_A k_B}{(k_A - k_B)(k_B - k_C)} e^{-k_B t} \\ - \frac{N_0 k_A k_B}{(k_A - k_C)(k_B - k_C)} e^{-k_C t} \end{aligned} \tag{S7}$$

In the above equations, N_0 is the initial population of species A that is created by strong-field ionization. Fig. S5 shows the temporal evolutions of the various populations, computed

based on the rate constants given in Table S1 and after convolving with an instrument response function of 119-fs FWHM. Note that the observed ΔA_{iso} time trace at a specific x-ray probe photon energy E is related to the populations via

$$\Delta A_{iso}(E,t) \propto IRF(t) * H(t) \sum_{i=1}^{4} S_i(E) N_i(t) \tag{S8}$$

where $S_i(E)$ is the absorption spectrum of component i and $N_i(t)$ is the time-dependent population of component i. In the 526-eV region, only H_2O^+, OH^*, and OH are expected to contribute to the ΔA_{iso} signal. The OH^- absorption appears just to the red of the pre-edge feature around 534 eV (*46*).

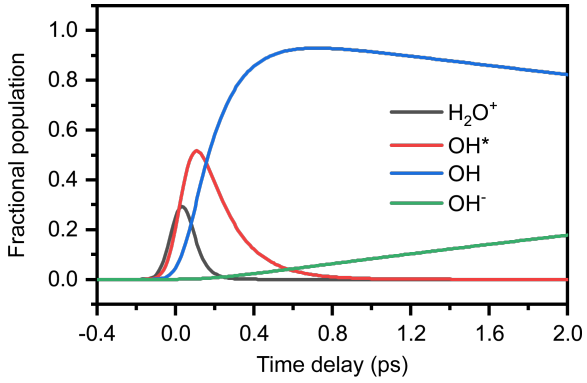

Figure S5: Sequential kinetics for $H_2O^+ \rightarrow OH^* \rightarrow OH \rightarrow OH^-$. $\tau_1 = 46$ fs, $\tau_2 = 0.16$ ps, $\tau_3 = 9.2$ ps.

4 Franck-Condon analysis of the OH absorption lineshape

The absorption spectrum of the OH radical (Fig. 2C) shows a sideband that is associated with the vibrational progression of the OH stretch, i.e., the main peak corresponds to the $v'' = 0 \rightarrow v' = 0$ transition whereas the vibrational sideband corresponds to the $v'' = 0 \rightarrow v' = 1$ transition. The amplitude of the sideband is $(0.139 \pm 0.028)\times$ that of the main peak, which implies a Huang-Rhys factor S of 0.139. (The Huang-Rhys factor characterizes the displacement between the potential energy curves of the electronic ground state and the O $1s^{-1}$ core-excited state.) Due to the difference in the OH bond length of H_2O^+ and OH, we expect the OH radical product to be initially formed in a vibrationally excited state. The Franck-Condon factors for transitions from the vibrationally excited $v'' = 1$ and $v'' = 2$ states of OH are summarized in Table S3; transitions from the $v'' = 0$ ground state are also included for comparison.

Based on the Franck-Condon factors, we compute the absorption lineshapes for the OH radical in the $v'' = 0, 1$, and 2 states (Fig. S6). The results obtained from the fit in Fig. 2C give the energy spacing between adjacent transitions of 0.48 eV and FWHM widths of each transition of 0.48 eV. Note that the absorption lineshapes for the vibrationally excited states of OH are significantly broader than that for the $v'' = 0$ ground state. Therefore, it is conceivable that the broader lineshape that is observed at early time delays in Fig. 2B arises from vibrationally hot OH. For comparison, we also include in Fig. S6 the lineshape of $S_1(E)$, modelled by a Lorentzian with a FWHM width of 0.98 eV.

Table S3: Franck-Condon factors for the various $v'' \rightarrow v'$ transitions of the OH radical.

	$v''=0$	$v''=1$	$v''=2$
$v'=0$	0.8700	0.1879	0.0084
$v'=1$	0.1211	0.6446	0.2097
$v'=2$	0.0084	0.3254	0.4651
$v'=3$	0.0004	0.0357	0.2713
$v'=4$	0.0000	0.0023	0.0418

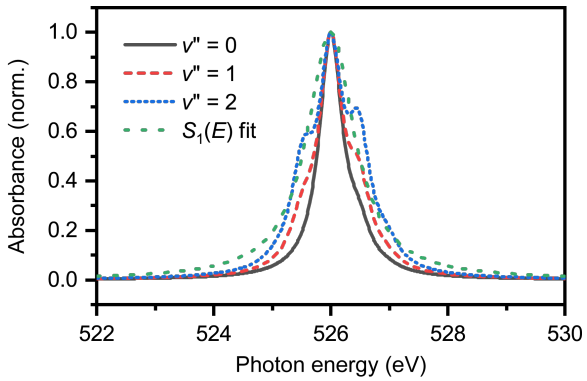

Figure S6: Calculated lineshapes for the OH radical in various vibrational states. The lineshape $S_1(E)$ that is obtained from the fit is also shown for comparison.

5 Pre-edge shift

In addition to observing the proton transfer and vibrational cooling dynamics of the H_2O^+ and OH radicals at 526 eV, we also observe a red-shift of the pre-edge on the sub-picosecond timescale (Fig. 2A). A single time constant τ effectively fits all the data over the entire probe photon energy range of 531.0 - 533.7 eV (Fig. S7), as described in the following expression

$$A(E,t) = S_0(E) + [S_1(E) + S_2(E)e^{-t/\tau}]H(t) * IRF(t). \tag{S9}$$

The origin of this absorption increase warrants further investigation with a thinner liquid microjet target that permits measurements beyond the main absorption edge at 537 eV. We

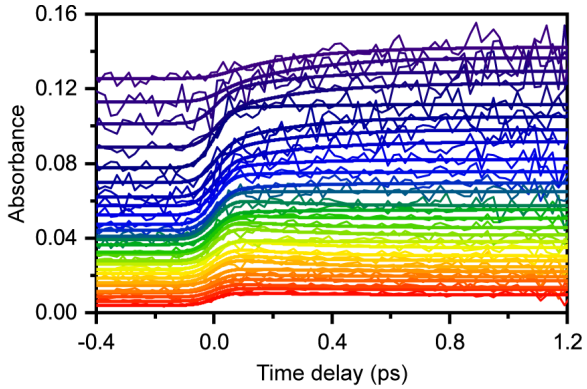

Figure S7: Differential absorption traces near the pre-edge resonance. The various traces, from red to violet, span 531.03 eV (red) to 533.73 eV (violet). All traces can be fit to a single time constant of 0.26 ± 0.03 ps.

exclude the possibility that the observed dynamics at the pre-edge is due to the H_2O^+ radical cation or the hot OH radical because the retrieved time constant $(0.26 \pm 0.03$ ps) is significantly different from the sub-picosecond time constants observed at 526 eV (46 ± 10 fs and 0.16 ± 0.03 ps) and our *ab initio* calculations (see Fig. 1B in the main text and Section 6 below) do not predict any x-ray absorption signature due to H_2O^+/OH in the pre-edge region. We also exclude the OH^- anion, which exhibits x-ray absorption resonances near the pre-edge (*46*), but the timescale for its formation due to geminate recombination is substantially longer, $\gtrsim 10$ ps. Hence, we posit that the spectral change observed at the pre-edge reflects the formation of the hydrated electron because of the agreement between the retrieved time constant and the $\sim$0.25-ps timescale for hydrated electron formation previously established by optical pump-probe spectroscopy (*7,8*). Hydrated electron formation is expected to disrupt the hydrogen bond network, which according to previous first-principles calculations (*47*) and infrared pump-soft x-ray probe (*48*) measurements of liquid water, results in an increase in the pre-edge x-ray absorption.

6 Theoretical Methods

Ab initio **molecular dynamics** To obtain an *ab initio* description of excited-state molecular dynamics of strong-field ionized water, we adopt a two-layered QM/MM approach, where a core region is treated quantum-mechanically (QM), and is embedded in a larger region described classically (MM) (*49*). We describe the electronic structure of a $(H_2O)_{12}^+$ cluster quantum-mechanically at the Hartree-Fock level of theory with the 6-31G Gaussian basis set. The QM cluster is embedded in 1012 additional water molecules described by the classical SPC/E water model (*50*). Internal bonds and angles in the MM region are constrained using the RATTLE algorithm (*51*). Within the QM/MM approach, the energy is given as

$$E(\vec{X}_{\mathrm{tot}}) = E_{\mathrm{QM}}(\vec{X}_{\mathrm{QM}}) + E_{\mathrm{MM}}(\vec{X}_{\mathrm{tot}}) - E_{\mathrm{MM}}(\vec{X}_{\mathrm{QM}}), \tag{S10}$$

where $\vec{X}_{\mathrm{tot}}$ comprises all nuclear coordinates and $\vec{X}_{\mathrm{QM}}$ the subset of nuclear coordinates in the QM region. The excited-state energies and gradients are obtained via Koopmans' theorem. For details, see Ref. (*27*).

To describe nuclear motion, we adopt Tully's fewest switches surface hopping (FSSH), which includes non-Born Oppenheimer effects (*25*). We sample over trajectories from a total of 107 snapshots that were obtained from long, thermostated trajectories. For each snapshot, we consider electronic states within the top 1.5 eV of the valence MO band to account for strong-field ionization.

X-ray absorption spectra X-ray absorption spectra are calculated at the same level of electronic structure theory as used for the molecular dynamics. The absorption cross section is given as

$$\sigma(\omega) = \frac{4}{3}\pi^2\omega\alpha \sum_{d=x,y,z} |\langle\phi_f|d|\phi_i\rangle|^2 \, \mathcal{V}(\omega - \omega_{\mathrm{res}}), \tag{S11}$$

where $\omega_{\mathrm{res}} = \epsilon_f - \epsilon_i$. Here, ϵ_i and ϵ_f refer to the initial and final MO energies, $\langle\phi_f|d|\phi_i\rangle$ are the transition dipole matrix elements, and α is the fine structure constant. We take the natural line width and the IRF into account with a Voigt profile $\mathcal{V}$, comprising a Lorentz function with a FWHM of 170 meV and a Gaussian function with a FWHM of 100 meV. The 2D spectrum in Fig. 3A of the main text is additionally convolved in time with a Gaussian function of 10 fs FWHM.

Identification of OH formation In order to identify the formation of OH in the trajectories, we employ bond-order analysis (*28*). The bond order of a given oxygen atom to its nearest two hydrogen atoms in the QM region is denoted as $b_{\mathrm{H1}}, b_{\mathrm{H2}}$, respectively. In $\mathrm{H_2O}$ and $\mathrm{H_2O^+}$, we expect $b_{\mathrm{H1}} \approx b_{\mathrm{H2}}$. To derive a criterion for OH formation, we demand that *(i)* the initial state is reproduced (no OH is present), *(ii)* the final proton transfer status after 200 fs is reproduced, and *(iii)* at any given time step, there is at maximum one OH per trajectory. With this, we establish OH formation if

$$b_{\mathrm{H2}}/b_{\mathrm{H1}} < 0.45. \tag{S12}$$

Identification of the OH allows us to study its diffusion towards the MM region (Fig. S8). While the radius of gyration,

$$r_{\mathrm{gyr}}^2 = \frac{\sum_{k=1}^{N_{\mathrm{atoms}}} m_k \left|\vec{r}_k - \vec{R}_{\mathrm{COM}}\right|^2}{\sum_{k=1}^{N_{\mathrm{atoms}}} m_k}, \tag{S13}$$

of the $(\mathrm{H_2O})_{12}^+$ QM cluster varies little over the course of 200 fs, the distance of the OH to the center of mass (COM) of the remaining QM region increases upon OH formation. Note that OH is formed initially close to the surface of the QM cluster. The OH to COM distance surpasses r_{gyr} after 80 fs. This is accompanied by a linear drift in the spectrum peak position. Therefore, we conclude that this linear drift is an artefact of the limited QM cluster size that enforces OH diffusion.

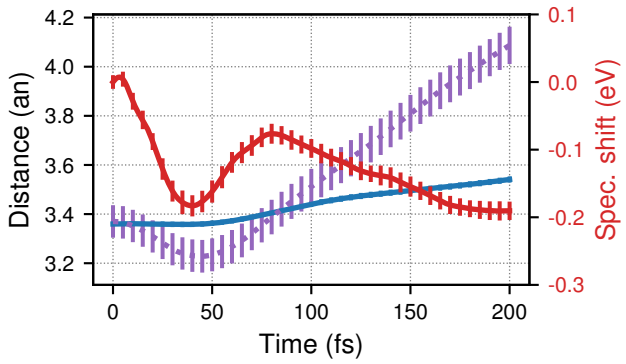

Figure S8: Analysis of distances within the $(H_2O)_{12}^+$ cluster. Radius of gyration of the QM region (blue) and distance of the OH to the COM of the QM region (purple). The shift of the spectrum peak position is included (red).

Hole and charge center The distance between the hole center and the charge center is a means of quantifying the progress of the proton transfer (cf. Ref. (*15*)). The hole can by Koopmans' theorem be identified with a Hartree-Fock molecular orbital α. Its center is given by

$$\vec{R}_H^{(\alpha)} = \sum_{k=1}^{N_{\text{atoms}}} G_k^{(\alpha)} \vec{r}_k, \tag{S14}$$

where $G_k^{(\alpha)}$ is the normalized weight of MO α at atom k. The charge center is located at

$$\vec{R}_C = \sum_{k=1}^{N_{\text{atoms}}} \left(q_k^{(\text{MC})} - q_k^{(\text{WM})} \right) \vec{r}_k, \tag{S15}$$

with the Mulliken charges $q_k^{(\text{MC})}$ and the water model charges $q_k^{(\text{WM})}$, where $q_{\text{O}}^{(\text{WM})} = -0.8476$, $q_{\text{H}}^{(\text{WM})} = +0.4238$. Since the charges on the OH are not adequately described within the water model, we exclude the OH from the summation in Eq. (S15).

Hole localization Hole localization for a valence hole in orbital α is measured by the hole radius $r_H^{(\alpha)}$, which is calculated analogously to a radius of gyration as

$$r_H^{(\alpha)} = \sqrt{\sum_{k=1}^{N_{\text{atoms}}} G_k^{(\alpha)} \left| \vec{r}_k - \vec{R}_H^{(\alpha)} \right|^2}. \tag{S16}$$

Core and valence MOs The position of the absorption peak is governed by the energy difference between the participating molecular orbitals. Fig. S9 shows the density of valence and core molecular orbitals over time. The orbitals that dominate the absorption (located at H_2O^+/OH) are highlighted by white lines. While the overall distribution of both valence and core orbitals broadens with time, there is a clear separation of the OH orbitals towards higher orbital energies ε_{MO}. Since this shift is comparable for valence and core orbitals, the overall spectral shift is comparatively small with a maximum of about 20 meV.

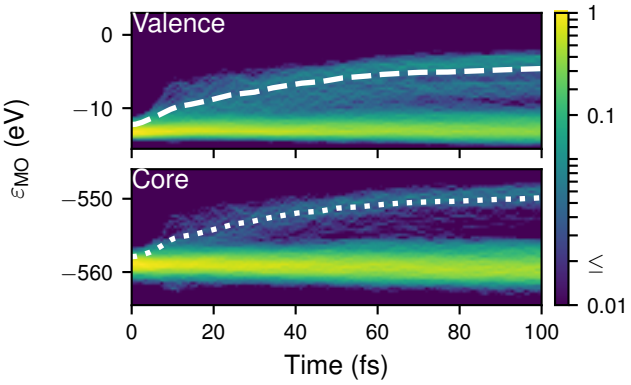

Figure S9: Density of valence (top) and core molecular orbitals (MOs) (bottom). MOs with dominant contribution to absorption spectrum highlighted (white lines).

Basis set effects The *ab initio* molecular dynamics simulations and x-ray absorption spectra presented in the main text were obtained using the 6-31G Gaussian basis set. By adding diffuse functions to the basis set, as was done in the gas phase spectra of Fig. 1B of the main text, the description of OH orbitals is improved and thus the x-ray absorption spectrum is affected. To study the effects of the basis size, while keeping the existing molecular dynamics trajectories, we calculated x-ray absorption including diffuse functions within the 6-31+G basis set. The resulting 2D spectrum is shown in Fig. S10. It corresponds to Fig. 3A of the main text and exhibits a blueshift of the spectrum at long times.

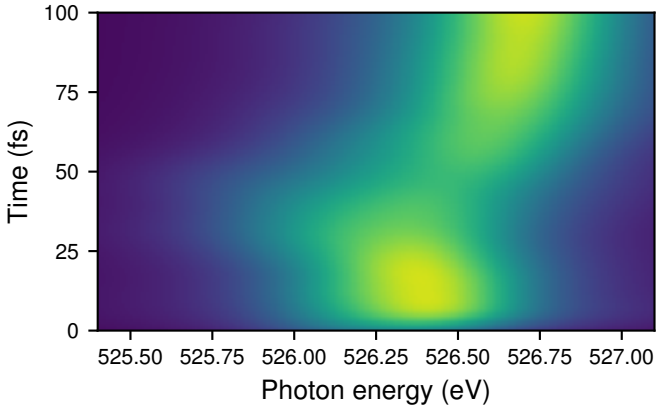

Figure S10: Two-dimensional x-ray absorption spectrum as in Fig. 3A of the main text, but calculated with the 6-31+G basis set which includes diffuse basis functions.

In order to resolve the difference between Figs. 3A (main text) and S10, in Fig. S11, we study the effect of including diffuse functions for the x-ray absorption spectrum of OH and $\mathrm{H_2O^+}$ in the gas phase. We find that, while the OH absorption line is redshifted with respect to the $\mathrm{H_2O^+}$ absorption line with the 6-31G basis set, a blueshift is observed for the 6-31+G basis set. This is consistent with the blueshift seen in Fig. S10 for long times, when proton transfer is completed and absorption is taking place mainly at the OH.

With the computational limitations that come with the *ab initio* treatment of an $(\mathrm{H_2O})_{12}^{+}$ QM cluster, molecular dynamics trajectories with the 6-31+G basis set are not feasible. (Please note that, unlike e.g. Ref. (*15*), we include non-adiabatic effects in our simulations.) However, based on the comparison in Fig. S11, we find that the x-ray absorption spectrum is sensitive to the decreasing distance between neighboring oxygen atoms (Fig. 3D, main text). The energy difference of about 1.0 eV between the x-ray absorption lines of OH in the 6-31G and the 6-31+G basis, respectively, arises mainly from the lowering of the oxygen core orbital when diffuse functions are introduced. The valence orbital, which is relevant for the molecular dynamics, is less affected.

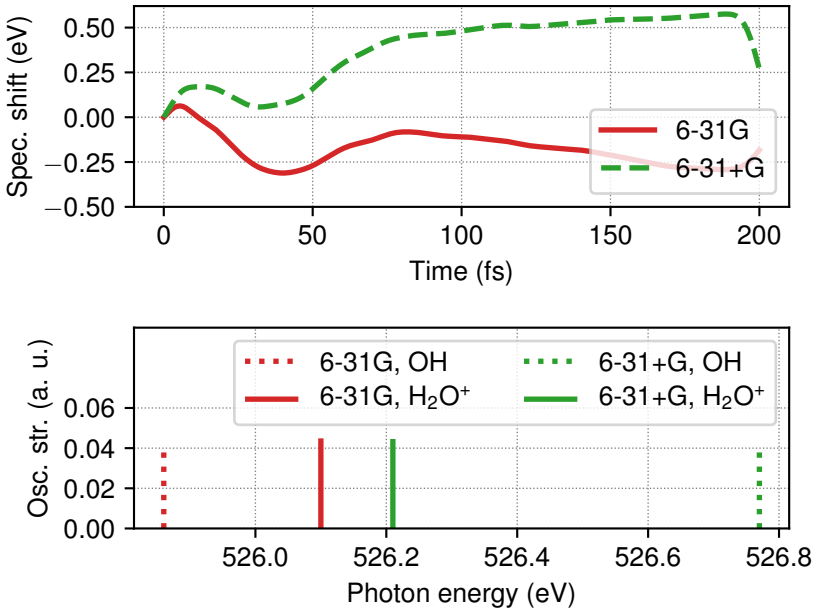

Figure S11: Comparison of x-ray absorption spectra obtained using the 6-31G and 6-31+G basis sets. *Top panel:* Position of the x-ray absorption peak over time. *Bottom panel:* Gas phase spectra of OH and H_2O^+.